Switchable Wavefront of Mid-Infrared Wave Using GeSbTe Metasurfaces

Hongyuan Zhu and Zhengyong Song

Abstract—**Benefiting from the unprecedented superiority of phase change material on manipulating electromagnetic wave, germanium antimony telluride-based optical devices attract a lot of attention. Here, based on Pancharatnam-Berry phase, reflective metasurfaces are presented by using phase change material-germanium antimony telluride ($Ge_3Sb_2Te_6$). They can manipulate reflection mode of terahertz wave and realize some functions. In order to verify this, three examples are numerically demonstrated, and they are gradient metasurface, vortex beam generator, and focusing lens. First of all, $Ge_3Sb_2Te_6$ blocks are used to construct reflective wavefront of gradient metasurface, and then realize switching between anomalous reflection and mirror reflection. Secondly, vortex beam generators are designed with $|l| = 1$ and $|l| = 2$, and mode number of orbital angular momentum is reconstructed through the switching of $Ge_3Sb_2Te_6$ between crystalline state and amorphous state. Finally, a reflective lens is presented, whose focus appears or disappears under different circular polarizations. By adjusting phase state of $Ge_3Sb_2Te_6$, dynamic adjustment of focusing intensity is realized. Our design may have potential applications in the fields of terahertz switching and communication.**

Index Terms—**GeSbTe, metasurface, anomalous reflection, orbital angular momentum, Lens.**

I. INTRODUCTION

ELECTROMAGNETIC metamaterials refer to artificially three-dimensional engineered materials. The combination of specific metal or dielectric structures can realize the manipulation of reflected and transmitted electromagnetic waves. Through some specific arrays, metamaterials realize many novel properties that natural materials do not own, such as negative permeability [1], [2] and negative refractive index [3], [4]. More electromagnetic responses are presented with charming phenomena, such as perfect imaging [5], [6] and invisible cloak [7], [8].

There are some defects in traditional electromagnetic metamaterials, such as large size, high loss, and expensive fabrication cost, and these problems limit the application range of electromagnetic metamaterials to a certain extent. As a two-dimensional planar structure of electromagnetic metamaterial, the appearance of metasurface effectively solves the above problems on the premise of maintaining basic characteristics of metamaterial. Metasurface has ultra-thin characteristic, is easier to process and integrate with devices, and has a wider range of applications. In 2012, Yu *et al.* demonstrated an optically thin metasurface that generates high-quality circularly polarized light over a broad wavelength range from 5 μm to 12 μm [9]. In 2015, Miao *et al.* proposed an ultra-thin reflective graphene metasurface with a wide phase modulation range. They used graphene as an adjustable loss to drive the transition from underdamped resonator to overdamped resonator [10]. In 2017, Li *et al.* presented a 1-bit coding metasurface to generate different high-resolution and low-noise holograms [11]. In 2018, Stav *et al.* used a dielectric metasurface to generate entanglement between spin and orbital angular momentum (OAM) of photons [12]. In 2020, shirmanesh *et al.* proposed tunable multifunctional metasurfaces that are capable of dynamic beam steering and reconfigurable light focusing [13]. In 2021, Zhang *et al.* reported a large-scale and reconfigurable nonvolatile metasurface based on phase change alloy $Ge_2Sb_2Se_4Te$. They demonstrated quasi-continuously tunable metasurfaces with large spectral tuning range [14].

Recently, active metasurface has aroused extensive research [15], [16]. Phase change materials have contrasting material properties in different states, and they would be an ideal material platform for the realization of active metasurfaces. Among phase change materials used for terahertz devices, the most popular choice is vanadium dioxide, and it is exploited for varied functionalities enabled by insulator-metal phase transition [17], [18]. However, practical use of vanadium dioxide in devices is hampered by its limited multi-level response and complexity of fabrication. In contrast, primary phases of germanium antimony telluride (GeSbTe), amorphous state and crystalline state, are stable for most applications. The state of GeSbTe can be thermally, optically or electrically switched at ultrahigh speed [19]. Furthermore, GeSbTe is extremely scalable and easily integrated [20], [21]. In 2013, Michel *et al.* demonstrated tuning of resonant frequency of aluminum nanoantenna by changing refractive index of $Ge_3Sb_2Te_6$ [22]. In 2015, Ríos *et al.* proposed nonvolatile multilevel memory based on $Ge_2Sb_2Te_5$, and realized up to eight levels of bit storage in a single device [23]. In 2016, Zheng *et al.* used ultra-thin $Ge_3Sb_2Te_6$ to realize reversible optical switch of highly confined phonon-polaritons [24]. In 2021, Abdollahramezani *et al.* presented a reconfigurable hybrid metasurface using $Ge_2Sb_2Te_5$ for active and nonvolatile tuning of light properties [25].
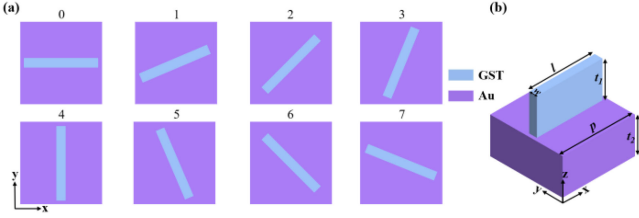
Fig. 1. (a) Top view of the proposed eight meta-atoms. (b) Three-dimensional meta-atom "0". Here, $t_1 = 0.5\ \mu m$, $t_2 = 0.5\ \mu m$, $l = 0.9\ \mu m$, $w = 0.1\ \mu m$, and $p = 1.0\ \mu m$, respectively.

In this work, switchable metasurfaces are proposed by $Ge_3Sb_2Te_6$ blocks. Based on Pancharatnam-Berry phase, the designed meta-atoms have 360° phase modulation ability by rotating azimuth angle of the top scatterer. Wavefront of meta-surface is reconfigurable and multiple functions are realized. In order to verify this, three examples are presented to demonstrate wavefront reconstruction. Firstly, the designed gradient metasurface is flexibly switched between anomalous reflection and mirror reflection when $Ge_3Sb_2Te_6$ is switched between crystalline state and amorphous state. Secondly, vortex beam generators are designed. In this case, phase state of $Ge_3Sb_2Te_6$ rebuilds mode number of OAM. Finally, we show a reflective metalens that switches dynamically between focusing and defocusing.

II. DESIGN AND MODEL

Pancharatnam-Berry phase, also known as geometric phase, was firstly proposed in optical system [26], [27]. Phase response is controlled by change in orientation rather than structural parameters of meta-atoms, which presents different geometric phases under irradiation of different circular polarizations (CPs). $Ge_3Sb_2Te_6$ metasurfaces are proposed based on Pancharatnam-Berry phase, and metasurfaces are composed of $Ge_3Sb_2Te_6$ blocks with different directional angles. Fig. 1(a) shows eight meta-atoms numbered 0–7, and rotation angle step of meta-atom is 22.5°. Each meta-atom is composed of gold film and $Ge_3Sb_2Te_6$ block. $Ge_3Sb_2Te_6$ has two states-crystalline state and amorphous state. Dielectric permittivity of crystalline state is $42.0 + 1.1i$, and that of amorphous state is $12.8 + 0.01i$ at 80 THz [22]. Drude model $\varepsilon(\omega) = \varepsilon_\infty - \frac{\omega_p^2}{\omega^2 + i\gamma\omega}$ is used to describe gold. In simulation, ε_∞ is 12, collision frequency γ is 1.05×10^{14} rad/s, and plasma frequency ω_p is 1.37×10^{16} rad/s. The details of three-dimensional meta-atom are presented in Fig. 1(b). Finite element method is employed to conduct full-wave simulation.

By adopting Pancharatnam-Berry phase, required phase is achieved. Fig. 2 shows amplitude and phase responses under incidences of left-handed circular polarization (LCP) and right-handed circular polarization (RCP) with different phase states of $Ge_3Sb_2Te_6$. As shown in Fig. 2(a) and (c), when $Ge_3Sb_2Te_6$ is in the crystalline state, phase difference between adjacent meta-atoms is always maintained at $\sim$45°. This condition ensures that Pancharatnam-Berry metasurface achieves 360° phase coverage and presents opposite phase response to LCP and RCP. In addition, amplitudes of eight meta-atoms are $\sim$0.9. In
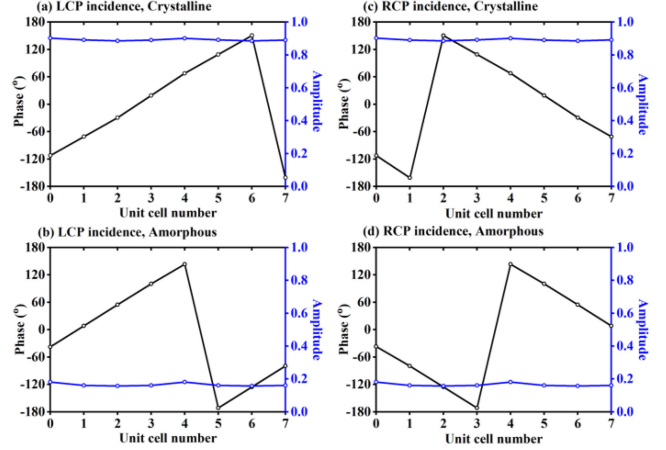

Fig. 2. Simulated amplitude and phase responses with $Ge_3Sb_2Te_6$ in crystalline (a and c) and amorphous states (b and d) under LCP (a and b) and RCP (c and d) incidence.
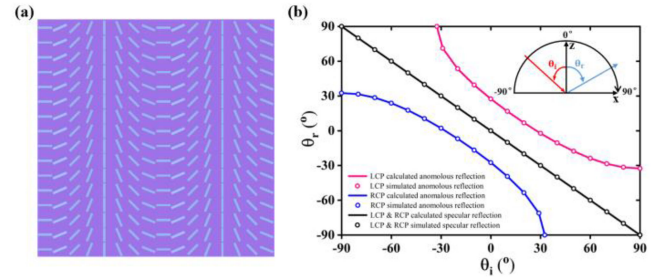

Fig. 3. (a) Top view of gradient metasurface. (b) Simulated and calculated reflection angles with different incident angles.

contrast, when $Ge_3Sb_2Te_6$ is in the amorphous state in Fig. 2(b) and (d), reflection phase still meets Pancharatnam-Berry phase, but reflection amplitude is generally reduced to less than 0.2 under incidences of LCP and RCP. Hence, change of reflection amplitude between crystalline state and amorphous state is used to dynamically manipulate reflected wavefront.

III. RESULTS AND DISCUSSIONS

A. Gradient Metasurface

According to the generalized Snell's law of reflection and refraction, direction of reflection wave is arbitrarily changed by introducing a suitable gradient phase (dΦ/dx) at interface [28], [29].

$$\sin(\theta_r)n_r - \sin(\theta_i)n_i = \frac{\lambda}{2\pi}\frac{d\Phi}{dx} \tag{1}$$

where θ_i is incident angle and θ_r is reflection angle. Gradient phase (dΦ/dx) is equal to $2\pi/8p$, and p is period of unit cell. The designed meta-atoms form metasurface with a certain phase gradient in Fig. 3(a). Such metasurface will provide an additional wavevector, which change wavefront of reflected beam. Fig. 3(b) shows simulated (circle) and calculated (line) reflection angles at different incident angles. When $Ge_3Sb_2Te_6$ is in the crystalline state, the phenomena of anomalous reflection are presented under incidences of LCP and RCP corresponding to pink curve and
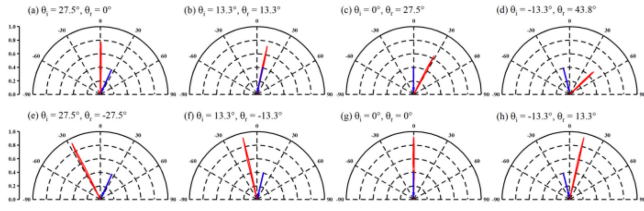
Fig. 4.   Normalized far-field power scattering pattern when LCP waves incident from 27.5°, 13.3°, 0°, and −13.3° at 80 THz, respectively. (a–d) Far-field scattering patterns with crystalline $Ge_3Sb_2Te_6$. (e,f) Far-field scattering patterns with amorphous $Ge_3Sb_2Te_6$.
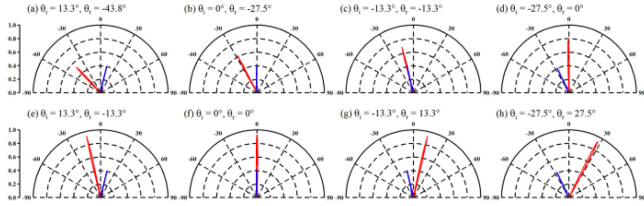

Fig. 5.   Normalized far-field power scattering pattern when RCP waves incident from 13.3°, 0°, −13.3°, and −27.5° at 80 THz, respectively. (a–d) Far-field scattering patterns with crystalline $Ge_3Sb_2Te_6$. (e,f) Far-field scattering patterns with amorphous $Ge_3Sb_2Te_6$.

blue curve in Fig. 3(b). Simulated results are in good agreement with calculated results. When $Ge_3Sb_2Te_6$ is in the amorphous state, it is seen from Fig. 2(b) and (d) that eight meta-atoms still cover 360°, but reflection amplitude is relatively low. As a result, mirror reflection occurs (black curve in Fig. 3(b)) and anomalous reflection is suppressed.

Figs. 4 and 5 represent normalized far-field scattering powers under incidences of LCP and RCP, and some interesting switching phenomena are found. When $Ge_3Sb_2Te_6$ is in the crystalline state, reflected waves exit from 0° when LCP/RCP wave is incident at +27.5°/−27.5° in Figs. 4(a) and 5(d). As shown in Figs. 4(e) and 5(h), phenomena of anomalous reflection are tuned to mirror reflection by switching $Ge_3Sb_2Te_6$ from crystalline state to amorphous state. Figs. 4(b) and 5(c) illustrate that when $Ge_3Sb_2Te_6$ is in the crystalline state, LCP/RCP at +13.3°/−13.3° will generate retroreflection, and reflected wave will return to original path. Mirror reflection occurs in Figs. 4(f) and 5(g) when $Ge_3Sb_2Te_6$ switches to amorphous state. When $Ge_3Sb_2Te_6$ is in the crystalline state, it is seen in Figs. 4(c) and 5(b) that reflection angles of normally incident LCP and RCP waves are +27.5° and −27.5°, respectively. When $Ge_3Sb_2Te_6$ is switched to amorphous state, incident wave return along $\theta_r = 0$° direction in Figs. 4(g) and 5(f). When $Ge_3Sb_2Te_6$ is in the crystalline state, anomalous reflection is emitted from +43.8°/−43.8° for LCP/RCP in Figs. 4(d) and 5(a), and efficiency is close to 56%. When $Ge_3Sb_2Te_6$ switches to amorphous state in Figs. 4(h) and 5(e), mirror reflection is 98%.

B. Vortex Beam Generator

OAM is a new degree of freedom in electromagnetic manipulation and is promising for channel multiplexing in communication system [30]. Recent years, vortex beam generators carrying OAM have received a lot of attention [31], [32]. Spin-controlled
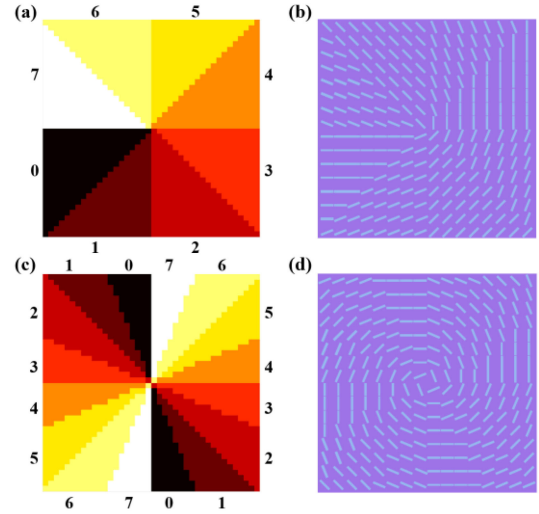

Fig. 6.   Phase distributions of vortex beam with $|l| = 1$ (a) and $|l| = 2$ (c). Meta-atom distributions of vortex beam generator with $|l| = 1$ (b) and $|l| = 2$ (d).

vortex beams carrying OAM with different modes are used to encode information and increase communication capacity. As shown in Fig. 6, the proposed eight meta-atoms are used to generate vortex beams with different modes. Spiral phase distribution of vortex beam carrying OAM is $\Phi = e^{jl\varphi}$, where φ is azimuth angle and l is OAM mode number. A simple method for creating vortex beam is to introduce a spiral-like phase shift, and phase distribution is expressed as

$$\phi(x, y) = l\varphi = l \arctan(y/x) \qquad (2)$$

Phase distribution in Fig. 6(a) consists of eight sectors and each sector corresponds to a specific phase. Discrete phase step is ± 45° from a sector to another. Meta-atoms are arranged in Fig. 6(b), and they can realize LCP and RCP vortex beams. Vortex beam with OAM mode of $l = −1$ will be generated under LCP incidence. Under RCP incidence, vortex beam with OAM mode of $l = +1$ will be generated. Fig. 6(c) shows another metasurface, and it is divided into sixteen sectors. For LCP incidence, vortex beam is generated with OAM mode of $l = −2$. For RCP incidence, vortex beam is generated with OAM mode of $l = +2$. Fig. 6(d) is the corresponding structure diagram.

In simulation, LCP/RCP wave is assumed to illuminate the designed generators, and results of reflection fields are shown in Fig. 7. For LCP incidence, simulated results in Fig. 7(a) and (c) show that amplitude distribution has a hollow center when $Ge_3Sb_2Te_6$ is in the crystalline state. This is consistent with the characteristic of vortex beam. Phase distributions show 360° phase rotation in azimuthal direction for $l = −1$ and 720° phase rotation for $l = −2$. Reflection efficiencies of the proposed vortex beam generators are 83.6% for $l = −1$ and 83.3% for $l = −2$. When $Ge_3Sb_2Te_6$ is switched to amorphous state, vortex beam generator achieves OAM mode conversion from $l = −1$ or $l = −2$ to $l = 0$. Plane wave and uniform phase are observed. For RCP incidence, results in Fig. 7(b) and (d) show that amplitude distribution has a hollow center when $Ge_3Sb_2Te_6$ is crystalline. Phase distribution presents a spiral distribution, and changes
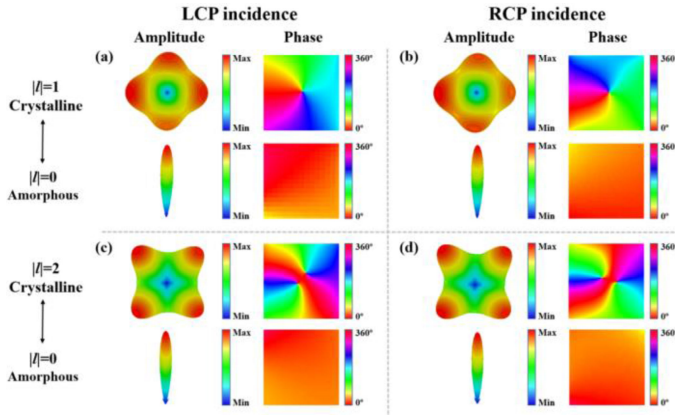
Fig. 7. Simulated amplitude and phase distributions of vortex beam generators with $l = \pm1$, 0, and ±2 under LCP incidence (a and c) and RCP incidence (b and d).
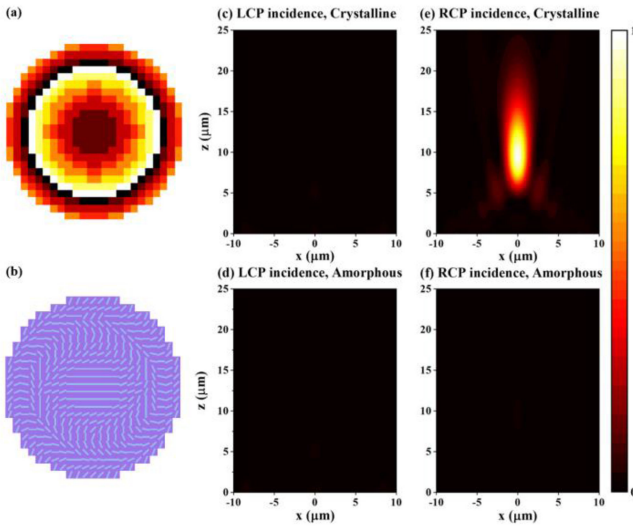

Fig. 8. Phase diagram (a) and structure diagram (b) of metalens. Power distributions for crystalline $Ge_3Sb_2Te_6$ (c) and amorphous $Ge_3Sb_2Te_6$ (d) under LCP incidence. Power distributions for crystalline $Ge_3Sb_2Te_6$ (e) and amorphous $Ge_3Sb_2Te_6$ (f) under RCP incidence. Results are normalized by the maximum value in (e).

once from $0°$ to $360°$ for $l = +1$ and twice from $0°$ to $360°$ for $l = +2$. Reflection efficiencies of the proposed vortex beam generators are 83.7% for $l = 1$ and 83.4% for $l = 2$. OAM beams with $l = +1$ and $l = +2$ are confirmed from both amplitude and phase distributions. When $Ge_3Sb_2Te_6$ switches to amorphous state, vortex beam generator realizes OAM mode conversion from $l = +1$ or $l = +2$ to $l = 0$.

C. Metalens

In order to design a focusing metalens, phase profile should meet

$$\varphi(x, y) = \frac{2\pi}{\lambda}(\sqrt{x^2 + y^2 + f_0{}^2} - f_0{}^2) \qquad (3)$$

where λ is wavelength in free space, f_0 is focal length, and (x, y) represents coordinates of meta-atom. Fig. 8(a) displays phase distribution of the designed metalens with the diameter

of 12 μm and a focal length of $f_0 = 10$ μm. Phase profile is discretized in a step of $45°$ in the x-y plane and represented with proper meta-atom in Fig. 8(b). Fig. 8(c) and (d) show intensity distributions when LCP wave is normally incident at 80 THz. Results show that metalens realizes defocus function regardless of phase state of $Ge_3Sb_2Te_6$. On the contrary, when $Ge_3Sb_2Te_6$ is in the crystalline state for RCP incidence, incident wave converges to focus at $z = 9.4$ μm. Full width at half maximum of focal point is 2.20 μm in Fig. 8(e). Focusing efficiency of metalens is 62.8%. When $Ge_3Sb_2Te_6$ switches to amorphous state, Fig. 8(f) illustrates that incident wave converges to focus at $z = 9.4$ μm. Full width at half maximum of focal point is 2.32 μm, and focusing efficiency is 1.7%. Therefore, the designed metalens realizes defocusing of LCP and focusing of RCP, and focusing intensity of RCP is dynamically adjusted by phase state of $Ge_3Sb_2Te_6$.

IV. CONCLUSION

In conclusion, switchable metasurfaces are presented based on $Ge_3Sb_2Te_6$ blocks to control electromagnetic wave. Based on Pancharatnam-Berry phase, the proposed meta-atoms have phase modulation ability of $360°$ and show opposite geometric phase for LCP and RCP incidences. When $Ge_3Sb_2Te_6$ is in the crystalline state, the overall reflection amplitude is $\sim$0.9, while $Ge_3Sb_2Te_6$ is switched to amorphous state, reflection amplitude decreases to less than 0.2. Therefore, the change of reflection amplitude is used to dynamically adjust the reflected wavefront. Gradient metasurface, vortex beam generator, and metalens are designed. It is found that the proposed gradient metasurface can switch between anomalous reflection and mirror reflection for different phase states of $Ge_3Sb_2Te_6$. In addition, OAM modes of vortex beam are $l = \pm1$, $l = \pm2$, and $l = 0$, and l is reconstructed by different states of $Ge_3Sb_2Te_6$. Finally, the designed metalens realizes focusing of RCP and defocusing of LCP, and focusing intensity of RCP is changed by switching between crystalline state and amorphous state of $Ge_3Sb_2Te_6$. Our work may provide a new perspective for the design of active metasurfaces.

REFERENCES

[1] T. J. Yen et al., "Terahertz magnetic resonance from artificial materials," Science, vol. 303, no. 5663, pp. 1494–1496, 2004.

[2] A. N. Grigorenko et al., "Nanofabricated media with negative permeability at visible frequencies," Nature, vol. 438, no. 7066, pp. 335–338, 2005.

[3] D. R. Smith, J. B. Pendry, and M. C. K. Wiltshire, "Metamaterials and negative refractive index," Science, vol. 305, no. 5685, pp. 788–792, 2004.

[4] J. F. Zhou, T. Koschny, L. Zhang, G. Tuttle, and C. M. Soukoulis, "Experimental demonstration of negative index of refraction," Appl. Phys. Lett., vol. 88, no. 22, 2016, Art. no. 221103.

[5] A. Grbic and G. V. Eleftheriades, "Overcoming the diffraction limit with a planar left-handed transmission-line lens," Phys. Rev. Lett., vol. 92, no. 11, 2004, Art. no. 117403.

[6] X. Z. Chen et al., "Dual-polarity plasmonic metalens for visible light," Nat. Commun., vol. 3, 2012, Art. no. 1198.

[7] U. Leonhardt, "Optical conformal mapping," Science, vol. 312, no. 5781, pp. 1777–1780, 2006.

[8] X. Ni, Z. Wong, M. Mrejen, Y. Wang, and X. Zhang, "An ultrathin invisibility skin cloak for visible light," Science, vol. 349, pp. 1310–1314, 2015.

[9] N. F. Yu, F. Aieta, P. Genevet, M. A. Kats, Z. Gaburro, and F. Capasso, "A broadband, background-free quarter-wave plate based on plasmonic metasurfaces," Nano Lett., vol. 12, no. 12, pp. 6323–6333, 2012.

[10] Z. Q. Miao *et al.*, "Widely tunable terahertz phase modulation with gate-controlled graphene metasurfaces," *Phys. Rev. X*, vol. 5, no. 4, 2015, Art. no. 041027.

[11] L. L. Li *et al.*, "Electromagnetic reprogrammable coding-metasurface hologram," *Nat. Commun.*, vol. 8, 2017, Art. no. 197.

[12] T. Stav, A. Faerman, E. Maguid, D. Oren, V. Kleiner, and E. Hasman, "Quantum entanglement of the spin and orbital angular momentum of photons using metamaterials," *Science,* vol. 361, no. 6407, pp. 1101–1104, 2018.

[13] G. K. Shirmanesh, R. Sokhoyan, P. C. Wu, and H. A. Atwater, "Electro-optically tunable multifunctional metasurfaces," *ACS Nano*, vol. 14, no. 6, pp. 6912–6920, 2020.

[14] Y. F. Zhang *et al.*, "Electrically reconfigurable non-volatile metasurface using low-loss optical phase-change material," *Nat. Nanotechnol.*, vol. 16, no. 6, pp. 661–666, 2021.

[15] C. H. Chu *et al.*, "Active dielectric metasurface based on phase-change medium," *Laser Photon. Rev.*, vol. 10, no. 6, pp. 986–994, 2016.

[16] A. M. Shaltout, V. M. Shalaev, and M. L. Brongersma, "Spatiotemporal light control with active metasurfaces," *Science*, vol. 364, no. 6441, 2019, Art. no. 648.

[17] Q. Q. Chu, Z. Y. Song, and Q. H. Liu, "Omnidirectional tunable terahertz analog of electromagnetically induced transparency realized by isotropic vanadium dioxide metasurfaces," *App. Phys. Exp.*, vol. 11, no. 8, 2018, Art. no. 082203.

[18] Z. Xu and Z. Song, "VO₂-based switchable metasurface with broadband photonic spin hall effect and absorption," *IEEE Photon. J.*, vol. 13, no. 4, Aug. 2021, Art. no. 4600305.

[19] D. Loke *et al.*, "Breaking the speed limits of phase-change memory," *Science*, vol. 336, no. 6088, pp. 1566–1569, 2012.

[20] F. Xiong, A. D. Liao, D. Estrada, and E. Pop, "Low-power switching of phase-change materials with carbon nanotube electrodes," *Science*, vol. 332, no. 6029, pp. 568–570, 2011.

[21] S. H. Lee, Y. Jung, and R. Agarwal, "Highly scalable non-volatile and ultra-lowpower phase-change nanowire memory," *Nat. Nanotechnol.*, vol. 2, no. 10, pp. 626–630, 2007.

[22] A. K. U. Michel *et al.*, "Using low-loss phase-change materials for mid-infrared antenna resonance tuning," *Nano Lett.*, vol. 13, no. 8, pp. 3470–3475, 2013.

[23] C. Ríos *et al.*, "Integrated all-photonic non-volatile multi-level memory," *Nat. Photon.*, vol. 9, no. 11, pp. 725–732, 2015.

[24] P. Li *et al.*, "Reversible optical switching of highly confined phonon–polaritons with an ultrathin phase-change material," *Nat. Mater.*, vol. 15, no. 8, pp. 870–875, 2016.

[25] S. Abdollahramezani *et al.*, "Dynamic hybrid metasurfaces," *Nano Lett.*, vol. 21, no. 3, pp. 1238–1245, 2021.

[26] M. V. Berry, "The adiabatic phase and pancharatnam's phase for polarized light," *J. Mod. Opt.*, vol. 34, no. 11, pp. 1401–1407, 1987.

[27] Z. Bomzon, G. Biener, V. Kleiner, and E. Hasman, "Space-variant pancharatnam-berry phase optical elements with computer-generated sub-wavelength gratings," *Opt. Lett.*, vol. 27, no. 13, pp. 1141–1143, 2002.

[28] N. F. Yu *et al.*, "Light propagation with phase discontinuities: Generalized laws of reflection and refraction," *Science*, vol. 334, no. 6054, pp. 333–337, 2011.

[29] S. L. Sun *et al.*, "High-efficiency broadband anomalous reflection by gradient metasurfaces," *Nano Lett.*, vol. 12, no. 12, pp. 6223–6229, 2012.

[30] L. Allen, M. W. Beijersbergen, R. J. C. Spreeuw, and J. P. Woerdman, "Orbital angular momentum of light and the transformation of Laguerre-Gaussian laser modes," *Phys. Rev. A,* vol. 45, no. 11, pp. 8185–8189, 1992.

[31] B. Wang *et al.*, "Generating optical vortex beams by momentum-space polarization vortices centred at bound states in the continuum," *Nat. Phonotics*, vol. 14, no. 10, pp. 623–628, 2020.

[32] M. Q. Mehmood *et al.*, "Visible-frequency metasurface for structuring and spatially multiplexing optical vortices," *Adv. Mater.*, vol. 28, no. 13, pp. 2533–2539, 2016.